Contact morphology and constitutive equation in evaluating tensile properties of austenitic stainless steels through instrumented spherical indentation

Young-Cheon Kim, Seung-Kyun Kang, Ju-Young Kim & Dongil Kwon

Journal of Materials Science
Full Set - Includes `Journal of Materials Science Letters'

ISSN 0022-2461

J Mater Sci
DOI 10.1007/s10853-012-6733-3

Springer

J Mater Sci
DOI 10.1007/s10853-012-6733-3

Contact morphology and constitutive equation in evaluating tensile properties of austenitic stainless steels through instrumented spherical indentation

Young-Cheon Kim · Seung-Kyun Kang · Ju-Young Kim · Dongil Kwon

Received: 1 June 2012 / Accepted: 9 July 2012

Abstract We evaluate representative stress and strain of austenitic stainless steels using instrumented indentation tests with a spherical indenter by taking into account the real contact depth and effective radius. We investigate the relation between material pileup underneath the spherical indenter and the strain-hardening exponent in uniaxial tensile tests for these steels. We evaluate the suitability of three constitutive equations, the Hollomon, Ludwigson, and Swift equations, for describing linear-type strain-hardening of austenitic stainless steels. Using the real contact depth and effective radii developed for the austenitic stainless steels, we find good agreement between representative stress and strain in instrumented indentation and uniaxial tensile tests.

Introduction

The instrumented indentation test (IIT), which measures load and displacement during indentation into a material with a rigid indenter [1–11], is widely used in structural applications and in materials and mechanical engineering research. Since IIT is nondestructive, it can be used to measure surface properties of in-field and in-use structures. It also can measure mechanical properties restricted to relatively small and local volumes, so that it is very useful in obtaining profiles or maps of mechanical properties in inhomogeneous materials. Further, it covers applications in wide ranges from macro to nano scales.

Many studies have been done to evaluate tensile properties using IIT [2–9] to measure tensile properties at small scales. One method is the representative stress and strain approach [2, 7–9], which directly correlates the stress–strain field underneath a spherical indenter to the stress–strain point in the uniaxial tensile test. In this approach, the representative stress σ_r is given by

$$\sigma_\mathrm{r} = \frac{P_\mathrm{m}}{\Psi} = \frac{1}{\Psi}\frac{L_\mathrm{max}}{A_\mathrm{c}}, \tag{1}$$

where P_m is the mean pressure, Ψ is the plastic constraint factor (about 3), L_max is the maximum indentation load, and A_c is the contact area at maximum load. The representative strain ε_r is expressed in the mathematical forms of sine or tangent functions

$$\varepsilon_r = \alpha \sin\gamma \text{ or } \varepsilon_r = \beta \tan\gamma, \tag{2}$$

where α and β are correlation constants and γ is the contact angle between the spherical indenter and the reference plane of material surface. Though the constraint factor and definition of strain depends on the material properties and its values are still in debate, some successful work has suggested useful combinations of representative stress and strain in some metallic materials: Tabor [9, 11], on the basis of extensive experiments, suggested the sine function-based representative strain, and Ahn and Kwon [12] suggested the tangent function which means shear strain at contact edge by considering the work-hardening characteristics. The flow curves and properties of ferritic steels that show power-law type strain hardening are successfully described using the tangent function in determining

---

Young-Cheon Kim and Seung-Kyun Kang contributed equally to this study.

Y.-C. Kim · S.-K. Kang · D. Kwon
Department of Materials Science and Engineering, Seoul National University, Seoul 151-744, Korea

J.-Y. Kim (✉)
School of Mechanical and Advanced Materials Engineering, UNIST, Ulsan 689-798, Korea
e-mail: juyoung@unist.ac.kr

Published online: 24 July 2012

representative strain [2]. On the other hand, Lee et al. [9] found that defining a sine function for representative strain is more suitable for austenite-based stainless steels in which the stress–strain hardening is linear.

As seen from Eqs. (1) and (2), the contact morphology in the loaded state should be determined precisely to define the representative stress and strain. The contact area A_c in spherical indentation is expressed from the contact depth h_c and indenter radius R as

$$A_c = \pi\left(2Rh_c - h_c^2\right). \tag{3}$$

Considering the elastic deflection depth h_d and the plastic pileup h_p, the real contact depth is given by

$$h_c = h_{max} - h_d + h_p. \tag{4}$$

Here h_d is determined by [1, 13, 14]

$$h_d = \varepsilon \frac{L_{max}}{S}, \tag{5}$$

where ε is the geometrical constant 0.75 for a spherical indenter and S is the initial unloading stiffness. Unlike elastic deflection, plastic pileup is not described in a form of analytical solution. As a primary parameter for pileup, early studies [7, 8, 14–17] proposed the yield strain (σ_y/E) where σ_y is the yield strength and E is the elastic modulus. For geometrically self-similar sharp indenters such as Berkovich, Vickers, and conical indenters, induced strain is a constant regardless of indentation depth, and the amount of plastic strain could be approximately inversely proportional to yield strain [13, 14]. For spherical indentation whose induced strain depends on indentation depth, previous works revealed that the yield strain has no direct relation to pileup and, for metallic materials, is related instead to the strain-hardening exponent n [13–19].

The strain-hardening exponent in the Hollomon equation generally determines the rate and amount of strain hardening during plasticity. For materials with high strain-hardening potential, the region right beneath the indenter, which is severely deformed, is much harder than deeper regions that are deformed less or not at all; since the hardened region can flow relatively easily downward, it piles up less upward, resulting in smaller material pileup. On the other hand, materials with low strain-hardening capability generally tend to pileup more [13, 18, 19]. On the basis of these concepts, Kim et al. [13] suggested the following empirical relation, taking account of the geometry of the spherical indenter based on finite-element analysis for 18 metallic materials:

$$h_c = (h_{max} - h_d)\left\{1 + 0.131\left(1 - 3.423n + 0.079n^2\right) \times \left(1 + 6.258\frac{h_{max}}{R} - 8.072\left(\frac{h_{max}}{R}\right)^2\right)\right\}. \tag{6}$$

This relation includes three insightful physical implications in spherical indentation: elastic deflection in the first term, hardening behavior represented by the strain-hardening exponent in the second term, and the geometrical effect of spherical indenter given by indentation depth and indenter radius in the third term.

The other parameter determining contact morphology is indenter radius, which is not always ideally spherical. Our previous research [20] suggested using the effective radius directly measured by a 3D profiler and an optical microscope. We showed that this approach is valid for metallic materials with power-law hardening behavior.

Here we determine representative stress–strain points for austenitic stainless steels using spherical IIT. A challenge is that austenite stainless steels show almost linear strain hardening, not power-law hardening, which means that the methodologies for determining contact depth and effective indenter radius described above could be incorrect. To derive exact representative stresses and strains for the austenitic stainless steels, we measure real contact depths by observing the residual impression with a 3D surface profiler. We find that previous methods are not valid for the austenitic stainless steels and suggest a modified mathematical form of contact depth for these steels. The effective radii are evaluated to calibrate the geometry of three spherical indenters. With the methods suggested for determining contact depth and effective indenter radius, we obtain representative stress–strains for four widely used austenitic stainless steels, STS304, STS304L, STS316L, and STS321, that agree well with stress–strain curves measured in uniaxial mechanical tests.

Experiments

Four austenitic stainless steels, STS304, STS304L, STS316L, and STS321, were prepared and specimen surfaces were polished with 1 μm Al_2O_3 powder. IITs were performed with an AIS 3000 portable indentation system (Frontics Inc., Korea), and maximum indentation depth was held at 100 μm with 10 partial unloadings and reloadings at every 10 μm indentation depth; the loading and unloading rates were 0.3 mm/min. After final unloading, the residual impressions were profiled with an optical interferometer (SIS series; SNU Precision, Korea) and pileup heights, h_p in Eq. (4), were measured by calculating the difference between the maximum peak of the residual impression and the undeformed reference surface. From the measured pileup heights, contact areas A_c in Eq. (3) were evaluated using Eqs. (3) and (4). Uniaxial tensile tests were carried out using an Instron 5582 (Instron Inc., USA) at cross-head speed of 1 mm/min; gauge length and diameter of cylindrical specimens were 25 and 6 mm, respectively, as per the ASTM standard [21].

Results and discussion

Contact depth

In the loaded state, contact depth is determined as a combination of elastic deflection (h_d) and plastic pileup (h_p) as shown in Fig. 1a. Elastic deflection is fully recovered after unloading, and pileup from the reference plane can be measured from the residual impression after unloading as shown in Fig. 1b, where h_f is the final indentation depth in the indentation load–displacement curve. Figure 2 shows a cross section of the residual impression for STS316L. The difference in height between the highest peak and reference plane is determined as the plastic pileup h_p. We calculated elastic deflection using Eq. (5), and the real contact depth h_c using Eq. (4) including plastic pileup. Figure 3 compares the ratio of h_c to h_{max}, the maximum indentation depth in Fig. 1a. This shows that contact depths evaluated by Eq. (6) for STS304, STS304L, STS316L, and STS321 are generally lower than the actual contact depths measured by 3D profile.

To investigate the effect of strain hardening on pileup in Eq. (6), we replace the term $(1-3.423n + 0.079n^2)$ in Eq. (6) by a material constant ω. Figure 4 shows the relation between ω and the strain-hardening exponent n. Equation (6), a straight line, predicts decreasing ω with increasing n, meaning that materials with high strain-hardening exponent

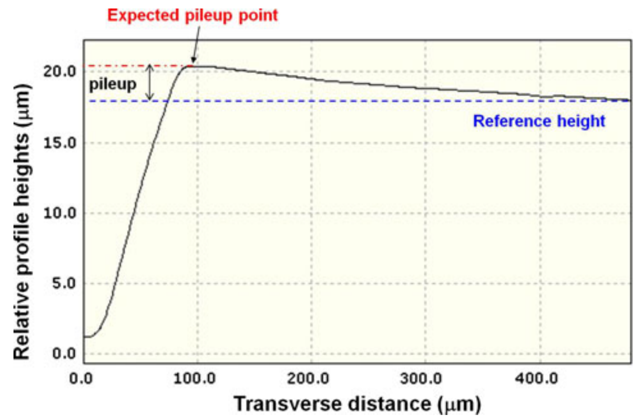

Fig. 2 Surface profile of residual impression for STS316L after spherical indentation with nominal radius 250 μm and maximum indentation depth 20 μm

tend to pileup less. The ω values of ferritic steels (STS410, SKS3, and SKH9) are on the solid line, by Eq. (6). However, the ω value for the stainless steels is independent of the strain-hardening exponent: the average value is 0.21 (±0.05) for STS321, STS304, STS304L, and STS316L whose strain-hardening exponent is above 0.23 as shown in Fig. 4. While Eq. (6) predicts sink-in phenomena for materials with n above 0.29 ($h_p < 0$), pileup behavior was observed for the austenitic stainless steels.

Constitutive equation

In general, the strain-hardening exponent is defined as in the Hollomon equation:

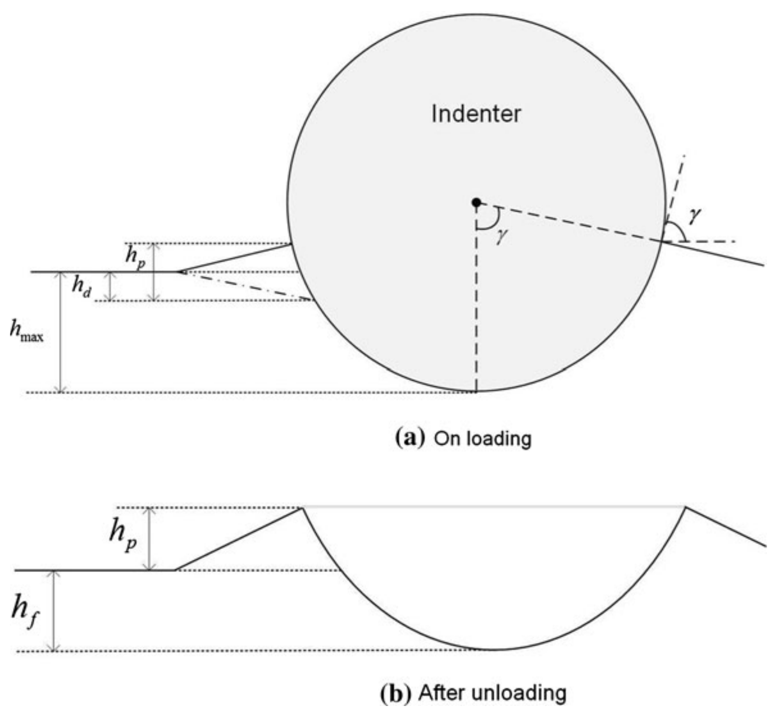

Fig. 1 Contact morphology of spherical indenter. **a** on loading, **b** after unloading

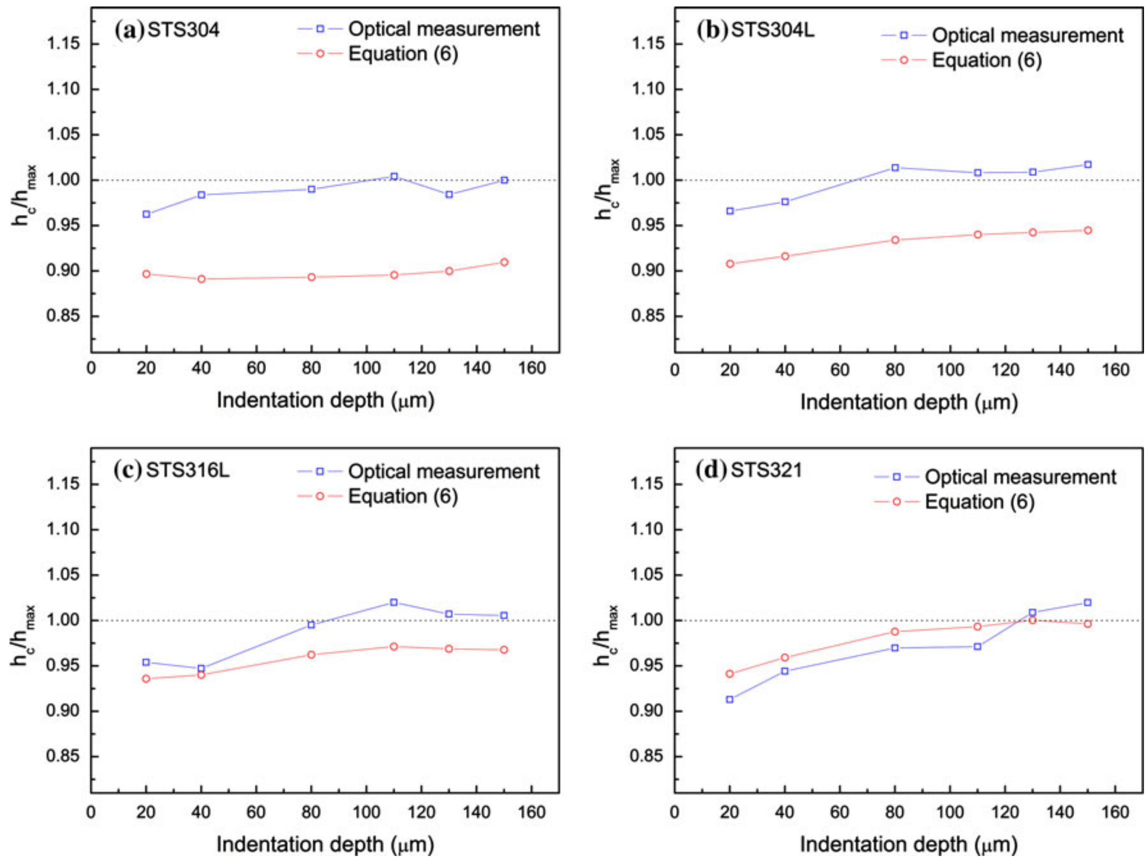

Fig. 3 The ratio of contact depth h_c, measured by profiling residual impressions and Eq. (6) to maximum indentation depth h_{max} for **a** STS304, **b** STS304L, **c** STS316L, and **d** STS321

$$\sigma = K\varepsilon^n, \tag{7}$$

where σ and ε is the flow stress and strain, and K is the strength coefficient [22, 23]. For austenitic stainless steels, however, the flow curve is almost linear rather than a power-law type, as shown in Fig. 5a where square dots were obtained from uniaxial tensile test for STS316L, so the Hollomon equation does not describe the entire flow curve for the austenitic steels (STS304, STS304L, STS316L, and STS321). The following equations have been suggested to describe a linear-type flow curve as in the austenitic stainless steels [24, 25]:

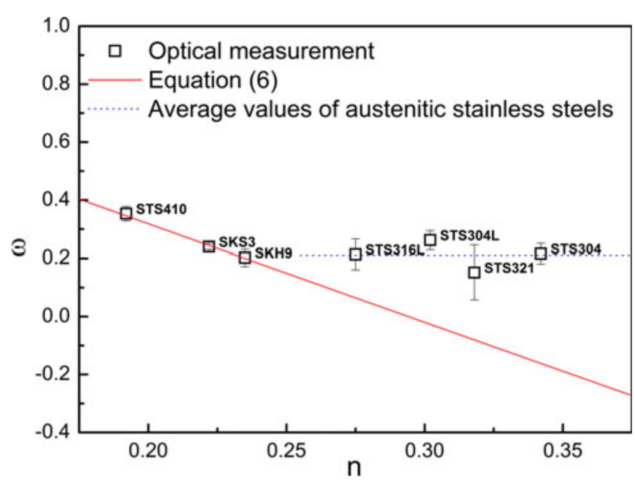

Fig. 4 ω as measured for ferrite (STS410, SKS3, SKH9) and austenitic steels (STS316L, STS304L, STS321, STS304) and as predicted by Eq. (6) as a function of strain-hardening exponent n

$$\sigma = K_{L1} \cdot \varepsilon^{n_{L1}} + \exp(K_{L2} + n_{L2} \cdot \varepsilon) \quad \text{(Ludwigson)} \tag{8}$$

$$\sigma = K_S(\varepsilon + \varepsilon_0)^{n_S} \quad \text{(Swift)}, \tag{9}$$

where K_{L1}, n_{L1}, K_S, n_S are constants corresponding to K, n in the Hollomon expression, K_{L2} and n_{L2} are Ludwigson's parameters describing the terms deviating from the Hollomon equation, and ε_o is Swift's constant. Ludwigson divided the linear-type strain hardening in austenitic stainless steel into two steps: a glide-dominant and a slip-dominant stages. Because austenitic stainless steels have relatively low stacking-fault energy, dislocations tend to dissociate into two partial dislocations, so that cross-slip, which requires combining partial dislocations, occurs less. This leads to more active planar glide and stronger strain hardening in the low-strain region. As the strain increases, mobile dislocations cross-slip relatively more and the flow

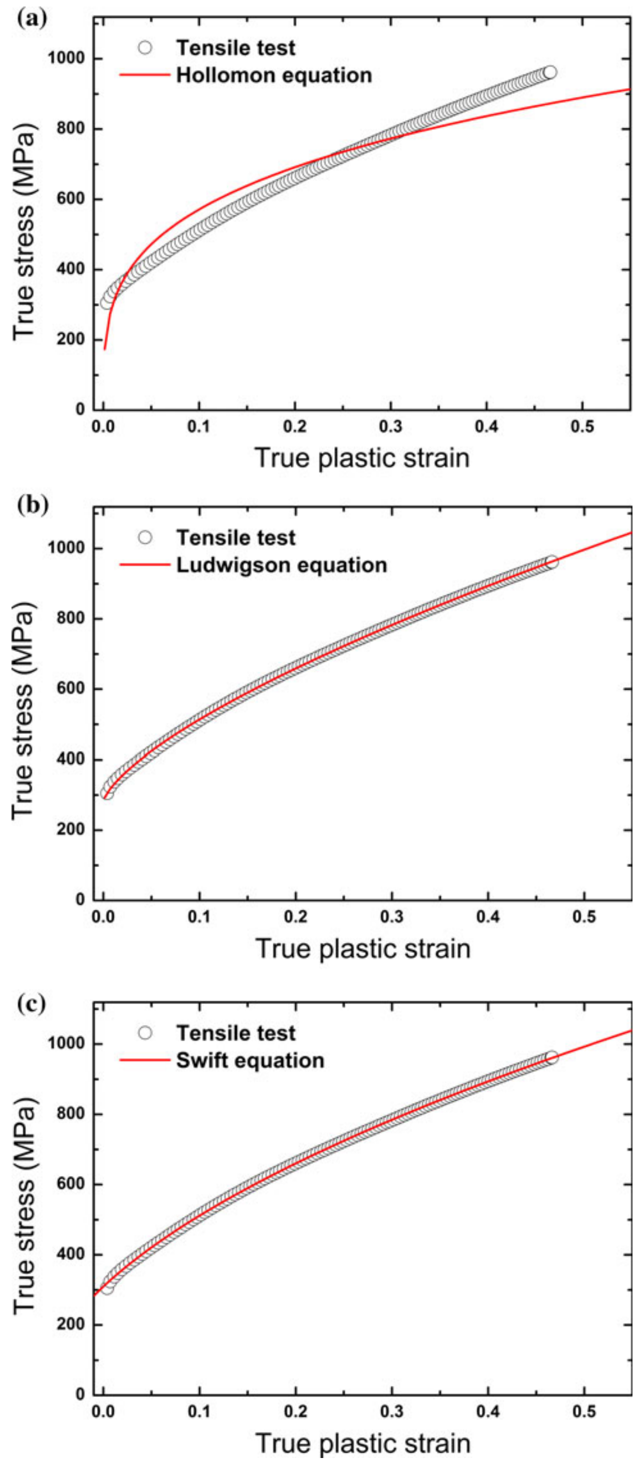

Fig. 5 True stress and plastic strain for STS316L and curves fitted to the tensile results by **a** Hollomon, **b** Ludwigson, and **c** Swift equations

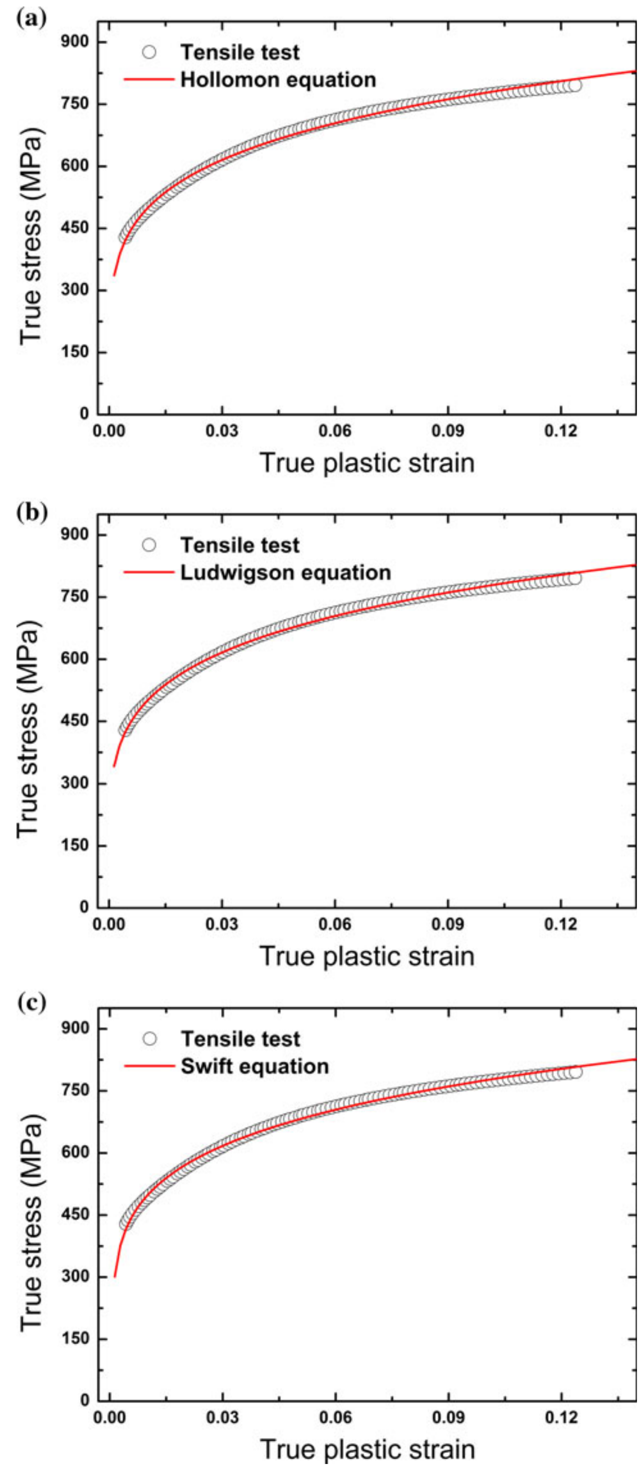

Fig. 6 True stress and plastic strain for STS410 and curves fitted to the tensile results by **a** Hollomon, **b** Ludwigson, and **c** Swift equations

curve gradually comes to steady state. Ludwigson described this linear hardening behavior by adding to the Hollomon equation the deviating term ($\exp(K_{L2} + n_{L2}\ \varepsilon)$) in the low-strain region, as in Eq. (8), to compensate for the strong strain hardening. Other research [26, 27] has shown that the deformation mechanism in austenitic stainless steel is related to competition between planar glide and cross slip. On the other hand, Swift [25] modified the Hollomon equation as in Eq. (9), suggesting the equivalent strain ε_0. The Swift equation was first introduced to calibrate uniform plastic strain by excluding non-uniform plastic strain,

Table 1 Coefficients in Hollomon, Ludwigson, and Swift equations

Material	Hollomon		Ludwigson				Swift		
	K (MPa)	n	K_{L1} (MPa)	n_{L1}	K_{L2}	n_{L2}	K_S (MPa)	ε_0	n_S
STS304	1306.46	0.3422	1082.80	0.7413	5.74	0.8226	1570.52	0.1128	0.7017
STS304L	1293.51	0.3021	1461.34	0.7121	5.76	−0.4567	1554.33	0.0661	0.5467
STS316L	1077.04	0.2752	1215.01	0.7074	5.64	−0.2110	1350.13	0.0650	0.5385
STS321	1069.92	0.3179	1198.78	0.7665	5.58	−0.1240	1321.84	0.0802	0.6096
SKH9	1454.45	0.2416	1383.80	0.2309	2.69	−0.7580	1238.96	0.0034	0.1824
SKS3	1247.20	0.2220	1243.59	0.2385	3.76	−4.2947	1111.43	0.0100	0.1653
STS410	1216.93	0.1944	1256.01	0.2406	4.47	−4.6790	1196.87	0.0007	0.1875

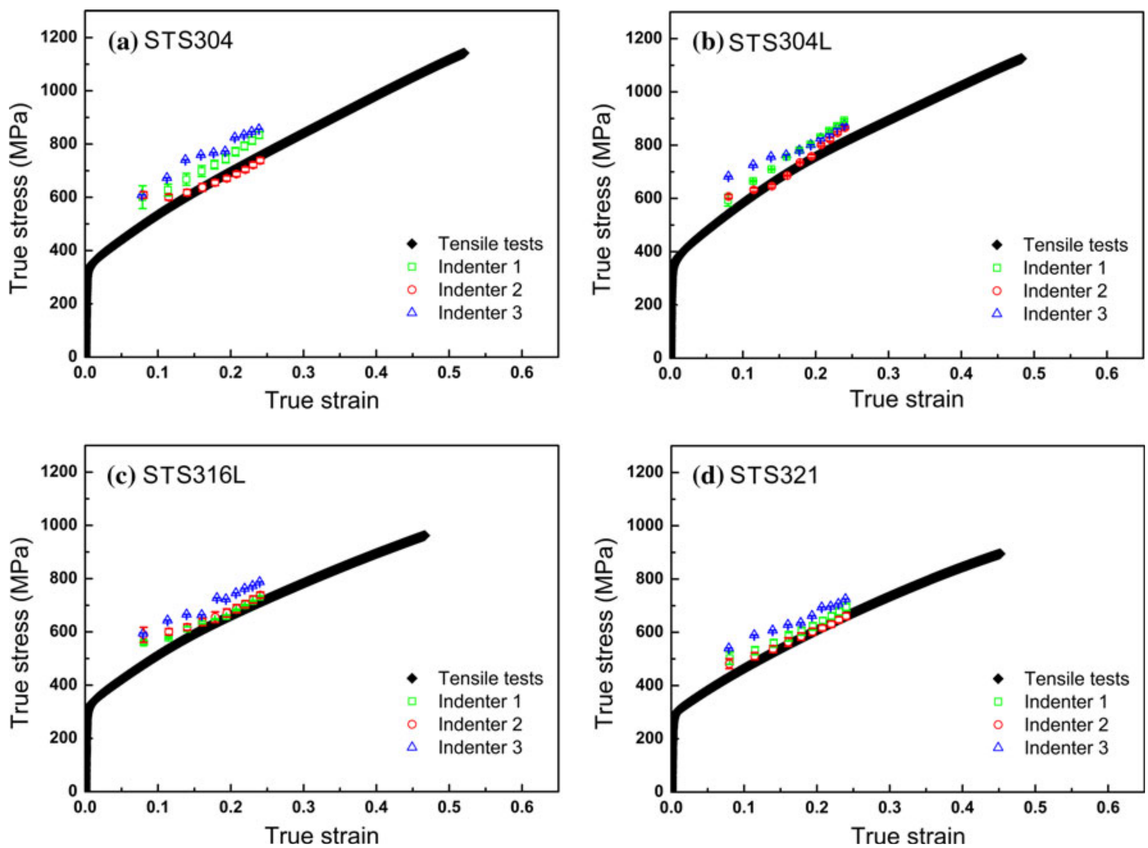

Fig. 7 Tensile curves and representative stress–strain points calculated by nominal indenter radius 250 μm for **a** STS304, **b** STS304L, **c** STS316L, and **d** STS321

such as non-uniform elongation in some carbon steels. However, this equation has been also used extensively to describe the tensile flow curve of materials with uniform elongation.

Figures 5, 6 show stress–strain data measured by uniaxial tensile tests for STS316L and STS410, respectively, and curves fitted to the tensile data by the Hollomon, Ludwigson, and Swift equations. The coefficients in these three constitutive equations when fitted to tensile stress–strain data for seven materials are summarized in Table 1. While the Hollomon equation fits tensile data for ferrite steels (SKH9, SKS3, STS410) successfully, it does not describe austenitic steels; on the other hand, the Ludwigson and Swift equations describe the tensile data for the seven materials well, as shown in Figs. 5, 6. Even though the Hollomon equation does not describe flow curves for the austenitic stainless steels for the entire strain region shown in Fig. 5, the strain-hardening indexes in the three equations, n, n_L, and n_S in Table 1, showed the same tendency for all seven materials.

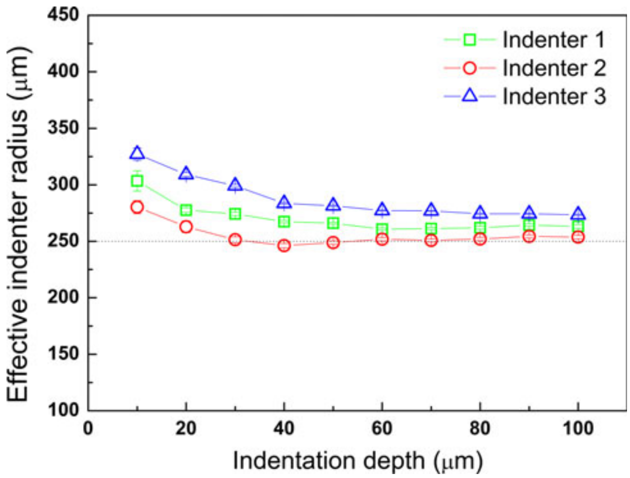

Fig. 8 Effective radii at various indentation depths derived from measured contact depth and area in Eq. (10)

Effective radius

For a spherical indenter, the indenter radius plays a critical role in determining the contact area as shown in Eq. (3). The spherical indenter is not always of constant radius for the entire indentation depth, so calibration for the imperfect geometry is required. In our previous work [20], an effective radius R_{eff} was proposed based on directly measured contact depth h_c and area A_c as

$$R_{\mathrm{eff}} = \frac{A_c/\pi + h_c^2}{2h_c}. \quad (10)$$

Since the proposed effective radius was verified for ferrite steels in which representative strain is described by a tangent function of the indenter angle, it is necessary to verify whether this effective radius is also valid for austenitic stainless steels, for which the definition of representative strain is a sine function of indenter angle.

We performed IITs using three different spherical indenters with nominal radius 250 μm. The three spherical indenters were made by same procedure, however, their effective radii could be slightly different. Figure 7 shows tensile data and representative stresses and strains evaluated with three indenters for STS321, STS304, STS304L, and STS316L. In Fig. 7, contact depths were determined using $\omega = 0.21$ in Eq. (6), and contact areas were evaluated with a nominal indenter radius of 250 μm. Representative stress was calculated from Eq. (1) and representative strain was $\beta \sin \gamma$ where β is 0.3 [9]. For the first two points at low strain, all three indenters

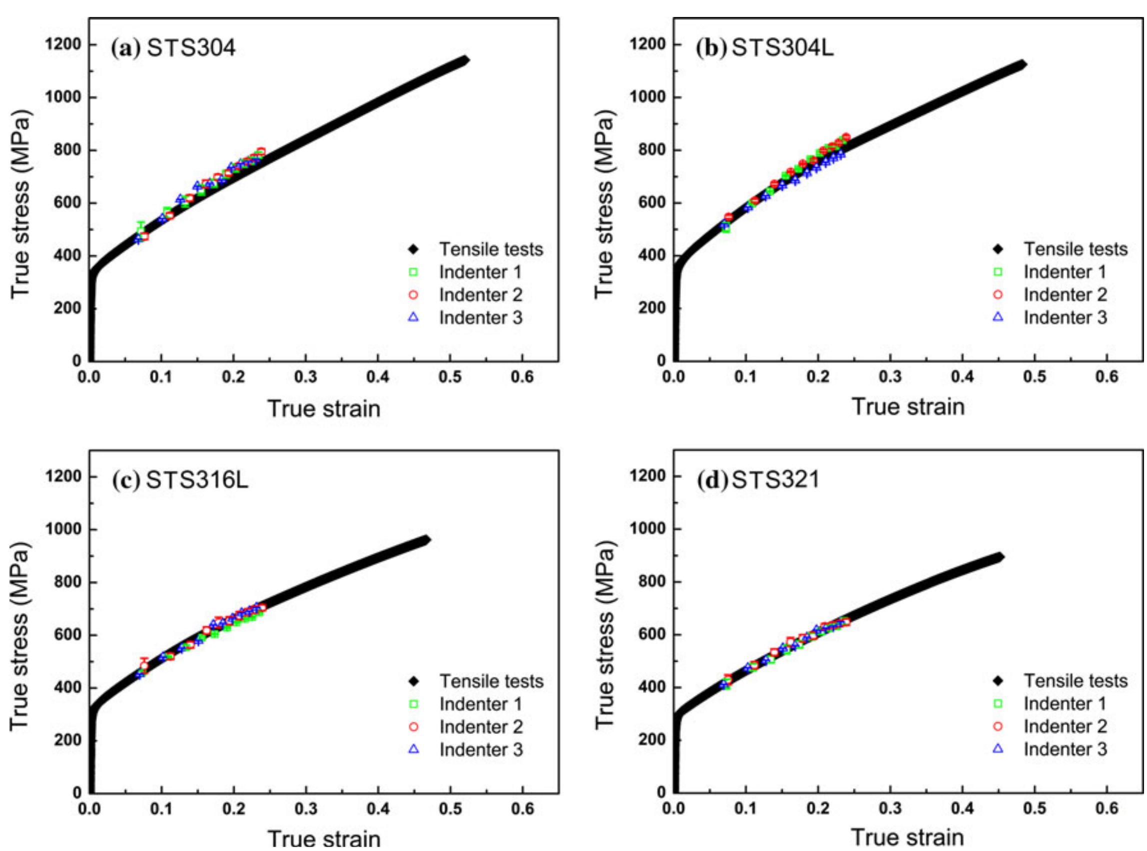

Fig. 9 Tensile curves and representative stress–strain points calculated by effective radius in Eq. (10) for **a** STS304, **b** STS304L, **c** STS316L, and **d** STS321

overestimate the representative stress, and representative stresses evaluated by indenter 2 tend to lie beyond tensile stress–strain curve.

To analyze the variation in representative stress and strain evaluated by the three indenters, we evaluated the effective radius defined by measured contact depth and contact area using Eq. (10). The effective radii of three indenters at various indentation depths were evaluated and are presented in Fig. 8, which demonstrates that the effective radii at shallow indentation depths are greater than the nominal radius. Figure 8 also shows that the effective radii of indenter 2 are very similar to the nominal radius 250 μm except for first two points at shallow indentation depths. We recalculated the representative stresses and strains using an indentation depth-dependent effective radius instead of a constant nominal radius, and we compared them to tensile data in Fig. 9. Figure 9 shows excellent agreement between tensile data and representative stresses and strains in spherical IIT. It also shows that the variation in real indenter shapes does not affect the representative stresses and strains. These results show that the representative stress and strain approach is valid for the austenitic stainless steels when representative strain is described by a sine function by calibrating geometry of indenter for the effective radius, and also show that the contact depth can be calculated correctly even when a constant nominal indenter radius does not describe the real radius for the entire range of indentation depths.

Conclusions

We evaluated representative stresses and strains of austenite stainless steels using spherical IITs. On the basis of the effects of the strain-hardening exponent n on pileup in the austenitic stainless steels, we used a constant of 0.21 instead of a function of n in Eq. (6) to calculate the real contact depth. We found that the flow curves of the austenitic stainless steels were described successfully by the Ludwigson and Swift equations rather than by Hollomon equation. We found that the approach using an effective radius defined by the real contact area and depth is valid for representative strains described by a sine function. Through these procedures, we accurately evaluated the representative stresses and strains of the austenitic stainless steels.

Acknowledgements This work was supported by the National Research Foundation of Korea (NRF) grant funded by the Korea government (MEST) (0417-20110083).

References

1. Oliver WC, Pharr GM (1992) J Mater Res 7:1564
2. Kim JY, Lee KW, Lee JS, Kwon D (2006) Surf Coat Technol 201:4278
3. Bouzakis KD, Michailidis N (2004) Thin Solid Films 469:227
4. Tyulyukovskiy E, Huber N (2006) J Mater Res 21:664
5. Klötzer D, Ullner C, Tyulyukovskiy E, Huber N (2006) J Mater Res 21:677
6. Lee YH, Kim Y, Park JS, Lee HM (2010) Nanosci Nanotechno Lett 2:337
7. Choi IC, Yoo BG, Kim YJ, Seok MY, Wang YM, Jang JI (2011) Scripta Mater 65:300
8. Lee YH, Park JS, Lee HM, Nahm SH (2010) Int J Mod Phys B 24:2453
9. Lee KW, Kim KH, Kim JY, Kwon D (2008) J Phys D Appl Phys 41:074014
10. Jang JI (2009) J Ceram Process Res 10:391
11. Tabor D (1951) Hardness of metals. Clarendon Press, Oxford
12. Ahn JH, Kwon D (2001) J Mater Res 16:3170
13. Kim SH, Lee BW, Choi Y, Kwon D (2006) Mater Sci Eng A Struct 415:59
14. Kang SK, Kim JY, Park CP, Kim HU, Kwon D (2010) J Mater Res 25:337
15. Malzbender J, de With G (2002) J Mater Res 17:502
16. Cheng YT, Cheng CM (1999) Int J Solids Struct 36:1231
17. Choi Y, Lee HS, Kwon D (2004) J Mater Res 19:3307
18. Alcalà J, Barone AC, Anglada M (2000) Acta Mater 48:3451
19. Bartier O, Hernot X, Mauvoisin G (2010) Mech Mater 42:640
20. Kang SK, Kim JY, Kang I, Kwon D (2009) J Mater Res 24:2965
21. ASTM E8-04 (2004) Standard test methods for tension testing of metallic materials. ASTM International, West Conshohocken
22. Hollomon JH (1945) Trans Metall Soc AIME 162:268
23. Kleemola HJ, Nieminen MA (1974) Metall Mater Trans 5:1863
24. Ludwigson DC (1971) Metall Mater Trans 2:2825
25. Swift HW (1952) J Mech Phys Solids 1:1
26. Samuel KG, Rodriguez P (2005) J Mater Sci 40:5727. doi: 10.1007/s10853-005-1078-9
27. Yoo JD, Park KT (2008) Mater Sci Eng A 496:417